

Neutron- and light-scattering studies of the liquid-to-glass and glass-to-glass transitions in dense copolymer micellar solutions

Wei-Ren Chen,¹ Francesco Mallamace,² Charles J. Glinka,³ Emiliano Fratini,⁴ and Sow-Hsin Chen^{1,*}

¹*Department of Nuclear Engineering, Massachusetts Institute of Technology, Cambridge, Massachusetts 02139-4307, USA*

²*Dipartimento di Fisica e Istituto Nazionale per la Fisica della Materia, Universita' di Messina, Villagio S. Agata, Caina Postal 55, I-98166 Messina, Italy*

³*NIST Center of Neutron Research, National Institute of Standards and Technology, Gaithersburg, Maryland 20899, USA*

⁴*Department of Chemistry and CSGI (Consorzio Sistemi a Grande Interfase), University of Florence, via della Lastruccia 3, I-50019, Florence, Italy*

(Received 9 May 2003; published 10 October 2003)

Recent mode coupling theory (MCT) calculations show that if a short-range attractive interaction is added to the pure hard sphere system, one may observe a new type of glass originating from the clustering effect (the attractive glass) as a result of the attractive interaction. This is in addition to the known glass-forming mechanism due to the cage effect in the hard sphere system (the repulsive glass). The calculations also indicate that if the range of attraction is sufficiently short compared to the diameter of the particle, within a certain interval of volume fractions where the two glass-forming mechanisms nearly balance each other, varying the external control parameter, the effective temperature, makes the glass-to-liquid-to-glass reentrance and the glass-to-glass transitions possible. Here we present experimental evidence of both transitions, obtained from small-angle neutron-scattering and photon correlation measurements taken from dense *L64* copolymer micellar solutions in heavy water. Varying the temperature in certain predicted volume fraction range triggers a sharp transition between these two different types of glass. In particular, according to MCT, there is an end point (called A_3 singularity) of this glass-to-glass transition line, beyond which the long-time dynamics of the two glasses become identical. Our findings confirm this theoretical prediction. Surprisingly, although the Debye-Waller factors, the long-time limit of the coherent intermediate scattering functions, of these two glasses obtained from photon correlation measurements indeed become identical at the predicted volume fraction, they exhibit distinctly different intermediate time relaxation. Furthermore, our experimental results obtained from volume fractions beyond the end point are characterized by the same features as the repulsive glass obtained before the end point. A complete phase diagram giving the boundaries of the structural arrest transitions for *L64* micellar system is given.

DOI: 10.1103/PhysRevE.68.041402

PACS number(s): 82.70.Dd, 61.12.Ex, 61.25.Hq, 64.70.Pf

I. INTRODUCTION

Observation of gelation phenomena in colloids, such as in protein gels or in gel-like emulsion-polymer mixtures, is a common experience in our daily life [1]. The gel state of a soft matter is characterized by an apparent manifestation of a drastic slowing down of the local structural relaxation dynamics around the typical particle in the system, which results in creation of a barrier for a dense, supercooled system to reach its true lowest free energy state, an ordered crystal-line solid. Instead, a nonergodic state or a “structurally arrested” state, in which the local particle configuration is deviated from the thermodynamical equilibrium state, is formed due to the short-range interaction potential between the particles. Although the structurally arrested state is an ubiquitous state of matter in our environment, traditionally this state of matter is rather ill-characterized physically: It is amorphous but classified neither as a gas or a liquid, nor as a crystal. Fortunately, recent progress [2] in the mode coupling theory (MCT) calculations opens up a possibility to gain a deeper physical insight into the detailed slow dynamical be-

havior of the system trapped in these structurally arrested states.

In the MCT, the structural arrest transition which causes the colloidal system to transform from a liquid state to an amorphous solid state is viewed as a result of a kinetic glass transition (KGT) predicted by the solution of the MCT bifurcation equation. The KGT has been studied extensively both experimentally and theoretically for a class of systems which can be modeled as a hard sphere system in the past two decades [3–5].

Many colloids can be modeled as a system of spherical particles interacting via a specific form of pairwise state-dependent effective pair potential. Therefore, the predictions of the MCT can be tested unambiguously by comparing various experimental results obtained from a colloidal system with results calculated explicitly using a specific interparticle potential. Initially, a hard sphere system with a purely repulsive interaction potential was used to model the colloidal system. At low volume fractions, the behavior of the colloidal system is fluidlike. As the volume fraction increases, the test-particle time correlation function [self-intermediate scattering function (self-ISF)] and the density-density correlation function (the intermediate scattering function) of the particles exhibit a two-stage relaxation process. The initial de-

*Electronic address: sowhsin@mit.edu

decay of the self-ISF corresponds to the rattling of a typical particle confined within a transient cage formed by its neighbors, followed by a slow decay, resulting from the relaxation of the cage itself and the escape of the trapped particle by rearranging its nearest neighbor configuration. The latter process leads to a possibility of particle diffusion through coupling to a structural relaxation process. If a system can be manipulated so as to avoid the known crystallization at the volume fraction of 0.495, for example by artificially creating a polydispersity in sizes of a few percent, at a critical volume fraction ϕ_c , which was predicted to be 0.516 (but determined to be 0.58 experimentally), the KGT can be observed [6]. At the KGT, both the particle diffusion and the long-time density fluctuations at all wavelengths freeze and the system undergoes an ergodic-to-nonergodic transition. Although this characteristic feature has been confirmed by computer molecular-dynamics simulations [7] and laboratory experiments [6,8] involving different glass formers, there have been some anomalous dynamical observations, which cannot be interpreted in terms of the theory based on the hard sphere potential alone [9].

A more complete picture of the KGT is obtained by modeling the interparticle potential more accurately. Recent MCT calculations [10–12] show that if a system is characterized by a hard core plus an additional short-range attractive interaction, for example, by an adhesive hard sphere system (AHS), a different dynamical arrest scenario emerges. Theoretically, the phase behavior of the AHS is characterized by an effective temperature $T^* = k_B T / u$, the volume fraction of the particles ϕ , and the fractional attractive well width $\varepsilon = \Delta / R$, where u is the depth of the attractive square well, Δ the width of the well, and R the diameter of the particle. In this case, for a given ε , aside from the volume fraction, as in the case of a pure hard sphere system, a second external control parameter, the effective temperature T^* , is introduced into the description of the phase behavior of the system and the loss of ergodicity can take place either by increasing the volume fraction or by changing the effective temperature.

Figure 1 shows part of the predicted phase diagram based on the AHS with $\varepsilon = 0.03$. In this case, it is possible for the system to undergo a reentrant (glass-to-liquid-to-glass) transition (for example at $\phi = 0.532$ in Fig. 1) by varying the effective temperature. At high effective temperatures and at sufficiently high volume fractions, the system evolves into the well-known structurally arrested (glassy) state, called a “repulsive glass,” as a result of the cage effect, a manifestation of the excluded volume effect due to the existence of the hard core. However, at relatively low effective temperatures, an “attractive glass” can form in which motion of the typical particle is hindered by the cluster formation with neighboring particles due to the short-range attractive interaction. Moreover, in an AHS, aside from the hard-core diameter, an additional length scale, the range of the attractive well, should come into play (parameter ε). With this insight, we may divide spherical colloidal systems into two categories: the one-length-scale hard sphere system, in which the glass formation is dictated by the cage effect alone; and the two-length-scale AHS, in which the two glass-forming mecha-

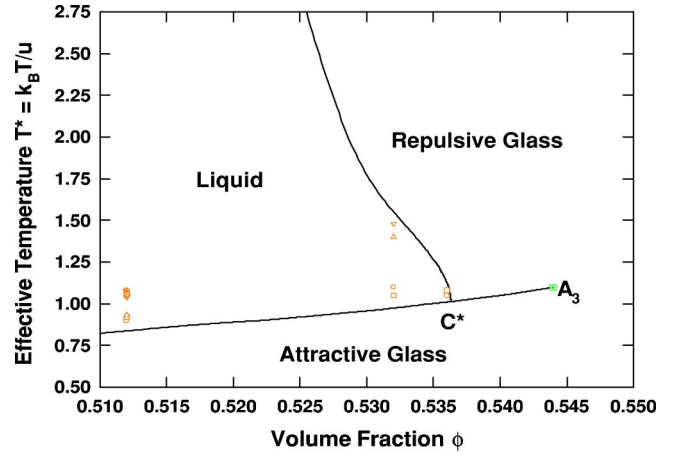


FIG. 1. (Color online) Theoretical phase diagram predicted by MCT calculations using the short-range attractive square-well potential with $\varepsilon = 0.03$. The calculations predict the attractive glass-to-liquid-to-repulsive glass reentrant transition, the attractive glass-to-repulsive glass transition, and the end point of the glass-glass transition line. Symbols (open circles, squares, and triangles) represent the effective temperature T^* , determined by fitting the experimental SANS data taken in the liquid state with the method explained in the text, for different volume fractions.

nisms may coexist and compete with each other, depending on the values of the controlled parameters. The MCT calculations show that, with sufficiently small ε , variation of the two control parameters T^* and ϕ allows the transition between these two distinct forms of glass. Thus there is a branch of the KGT line across which transitions between the attractive glass and the repulsive glass are predicted. Of particular interest is the occurrence of an A_3 singularity (see Fig. 1) at which point the glass-to-glass transition line terminates. MCT suggests that the long-time dynamics of the two distinct structurally arrested states become identical at and beyond this point.

Several ongoing experimental investigations have confirmed some of the theoretical predictions, such as the reentrant glass-to-liquid-to-glass transition phenomenon [13,14] and the logarithmic relaxation of the glassy dynamics in the liquid states in the vicinity of the A_3 singularity [15]. They are considered to be signatures of the glassy dynamics in the two-length-scale system. Yet, except for some recent experimental reports on a dense micellar system [16,17], a detail investigation of the glass-to-glass transition is just emerging, and the physical insight into the slow dynamics near its associated A_3 singularity still need to be clarified.

The study of KGT by neutron-scattering method is traditionally dominated by the use of the inelastic neutron-scattering (INS) and the spin-echo spectroscopy techniques. However, by analyzing an extensive set of small-angle neutron-scattering (SANS) intensity distributions obtained from $L64$ micellar solutions, which exposes all the characteristics of the AHS from our previous works [16,17], we demonstrated that SANS is also a suitable tool to investigate the boundary of the KGT: By analyzing SANS intensity distributions, the difference in the structure factor before and after the KGT can be visualized vividly. Supplemental to the

photon correlation spectroscopy (PCS), it provides rapid measurements of the peak of the structure factor over a wide temperature and volume fraction ranges, which is more difficult to do with INS or spin-echo spectroscopy. By this method, we successfully confirmed the predicted reentrant phenomenon, the glass-to-glass transition and most importantly, the existence of the A_3 singularity, in quantitative agreement with predictions of MCT. Furthermore, we are able, using SANS technique, to map out the complete structural arrest phase boundaries for the *L64* micellar system.

II. EXPERIMENT

The micellar system we study is a triblock copolymer *L64*, one member of the Pluronic family, used extensively in industrial applications. After necessary purification procedure [18] to remove hydrophobic impurities, the polymer is dissolved in deuterated water (D_2O). Pluronic is made of polyethylene oxide (PEO) and polypropylene oxide (PPO). The chemical formula of *L64* is $(PEO)_{13}(PPO)_{30}(PEO)_{13}$, having a molecular weight of 2990 Da. At low temperatures, both PEO and PPO are hydrophilic, so that *L64* chains readily dissolve in water, and the polymers exist as unimers. As the temperature increases there is a decrease in the probability of hydrogen-bond formation between water and polymer molecules, PPO tends to become less hydrophilic faster than PEO. This creates an unbalance of hydrophilicity between the end blocks and the middle block of the polymer molecule, and the copolymer molecules acquire surfactant properties in the aqueous environment and self-assemble to form micelles. Thus the micellar formation is initiated at a well-defined critical micellar temperature-concentration line. As the temperature further increases, water becomes progressively a poor solvent to both PPO and PEO chains, and the effective micelle-micelle interaction becomes attractive. The evidence for the increased short-range micellar attraction as a function of temperature comes from the existence of a lower consolute critical point at $C=5.0$ wt % and $T=330.9$ K [19] and a percolation line detected by a jump of zero-shear viscosity of more than two orders of magnitude [20]. We have explored the dynamically arrested states and their structure in this micellar system, as a function of temperature at high volume fractions. During the experiments the temperature stability was controlled to within ± 0.1 K.

SANS measurements were performed at NG7, a 40-m SANS spectrometer in the NIST Center for Neutron Research, and at SAND station at the Intense Pulsed Neutron Source (IPNS) in Argonne National Laboratory. At NG7, incident monochromatic neutrons of wave length $\lambda=5$ Å with $\Delta\lambda/\lambda=10\%$ were used. Sample to detector distance was fixed at 6 m, covering the magnitude of wave vector transfer (k) range 0.008 Å⁻¹– 0.3 Å⁻¹. At IPNS, high energy spallation neutrons are generated by bombarding a heavy metal target with repetitive pulses of 500 MeV protons. After moderation of these high energy neutrons by a solid methane moderator, a pulse of white neutrons was selected with an effective wave length range from 1.5 Å to 14 Å. In SAND all these neutrons are utilized by encoding their individual time of flight and their scattering angles determined by their detected

positions at a two-dimensional (2D) area detector. The 2D area detector has an active area of 40×40 cm² and the sample to detector distance is 2 m. This configuration allows a maximum scattering angle of about 9°. The reliable k -range covered in the measurements were from 0.004 Å⁻¹ to 0.6 Å⁻¹. k -resolution functions of both of these SANS spectrometers are Gaussian and well characterized. It is essential that we apply these resolution broadening to the theoretical cross section when fitting the intensity data. Sample liquid was contained in a flat quartz cell with 1 mm path length. The measured intensity was corrected for background and empty cell contributions, and normalized by a reference scattering intensity of a polymer sample of known cross section.

The photon correlation spectroscopy measurements were made at a scattering angle $\theta=90^\circ$, using a continuous wave solid state laser (Verdi-Coherent) operating at 50 mW ($\lambda=5120$ Å) and an optical scattering cell of a diameter 1 cm in a refractive index matching bath. The intensity data were also corrected for turbidity and multiple scattering effects. PCS data have been taken using a digital correlator with a logarithmic sampling time scale which allows an accurate description of both the short- and the long-time regions of the intermediate scattering function, from 1 μ s up to 100 s. Following the method used for colloidal hard spheres [8] we measure the correlation function

$$g^{(2)}(k, \tau) = \langle\langle I(k,0)I(k, \tau) \rangle\rangle / \langle\langle I(k,0) \rangle\rangle^2, \quad (1)$$

where $I(k, \tau)$ is the intensity of light scattered at wave vector k and at a delay time τ . The first bracket denotes the time average and the second bracket denotes the positional average over different parts of the sample. Since the system shows a structural arrest transition, and therefore a nonergodic behavior, particular care has been taken in averaging over many different positions in the sample for the measurement of the long-time part of the time correlation function. For each sample and each temperature we have performed more than 200 positional average measurements, observing a large scattering area corresponding to three or more independent Fourier components and changing the position of the sample in order to observe different scattering volumes. The ISF $g^{(1)}(k, \tau)$ can be obtained from Eq. (1) in a straightforward way using the Siegert relation.

III. SANS DATA ANALYSIS

The absolute intensity (in unit of cm⁻¹) of small-angle neutron scattering from a system of monodispersed micelles can be expressed by the following formula:

$$I(k) = cN \left[\sum_i b_i - \rho_w v_p \right]^2 \bar{P}(k) S(k), \quad (2)$$

where c is the concentration of polymer (number of polymers/cm³), N the aggregation number of polymers in a micelle, $\sum_i b_i$ sum of coherent scattering lengths of atoms comprising a polymer molecule, ρ_w the scattering length density of D_2O , and v_p the molecular volume of the poly-

mer. $\bar{P}(k)$ is the normalized intraparticle structure factor calculated by the modified cap-and-gown model [16] and $S(k)$ the intermicellar structure factor of a spherical particle system interacting via an attractive square-well potential with a repulsive hard core. $S(k)$ is calculated analytically by solving the Ornstein-Zernike (OZ) equation in Percus-Yevick approximation, for this square-well potential, to the first order in a series of small ε expansion [21]. The detailed analytical expression of $S(k)$ can be found in a previous publication [16]. It is important to note that the $\bar{P}(k)$ is the function of the aggregation number N only and $S(k)$ is the function of the aggregation number N , the volume fraction of micelles ϕ , the fractional well width parameter ε , and the effective temperature T^* . To fit SANS data in absolute intensity scale, it is essential to take into account the incoherent background and the resolution correction of the instrument used. The main point is that an absolute SANS intensity distribution in the liquid state can be fitted by Eq. (2) uniquely with four parameters: N , ϕ , ε , and T^* .

To illustrate the model fitting, a SANS intensity distribution obtained from a 48.5 wt.% micellar solution at 333 K in an absolute scale is shown in the upper panel of Fig. 2 as an example. Symbols give the experimental data and the dash line gives the model fitting taking into account the resolution correction. The same data plotted in a log-log scale are shown in the inset. It can be seen that for sufficiently large k , the SANS absolute intensity decreases as k^{-4} , in agreement with the Porod's law as expected in a two-phase system with a sharp interface. The lower panel shows the normalized intra-particle structure factor $\bar{P}(k)$ (circles) and the interparticle structure factor $S(k)$ (squares) for this case. The observed SANS data are proportional to the product of these two functions. The fact that the first diffraction peak of $S(k)$ occurs at a relatively smooth tail part of $\bar{P}(k)$ implies that the interaction peak in the SANS intensity distribution is primarily reflecting the width of the first diffraction peak of $S(k)$.

IV. SCALING PLOT OF SANS INTENSITY DISTRIBUTION

At high enough polymer concentration, SANS intensity distribution from the $L64/D_2O$ micellar system generally consists of a single, sharp interaction peak. Since there is a single peak in the observed SANS intensity distribution, we can assume that the system is characterized by a single length scale $\Lambda = 1/k_{\max}$ where k_{\max} is the peak position of the intensity distribution. It is well known that the absolute intensity in a two-phase system (the micelles and the solvent) is given by a 3D Fourier transform of the Debye correlation function $\Gamma(r)$, and the Debye correlation function in this case must be of the form $\Gamma(r/\Lambda)$ (scaling). Therefore

$$I(k) = \langle \eta^2 \rangle \int_0^\infty dr 4\pi r^2 j_0(kr) \Gamma\left(\frac{r}{\Lambda}\right), \quad (3)$$

where $\langle \eta^2 \rangle$ is the so-called invariant.

By making a transformation of variables,

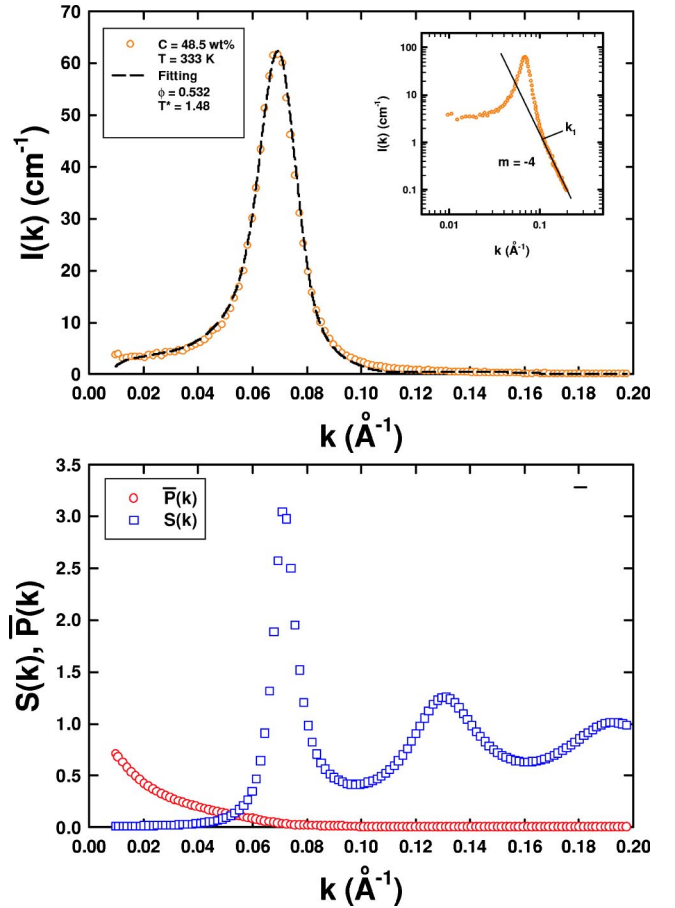


FIG. 2. (Color online) The upper panel shows the typical SANS intensity distribution in an absolute scale and its model fit taking into account the effect of resolution function. Symbols represent the experimental data and the dash line the theory convoluted with the resolution function. The inset gives the same data but plotted in a log-log scale. It can be seen that the Porod's law is satisfied at large k , as is expected in a two-phase system with a sharp interface. The lower panel gives the normalized intraparticle structure factor $\bar{P}(k)$ (circles) and the interparticle structure factor $S(k)$ (squares) used to fit the data in the upper panel. The $S(k)$ is calculated by solving the OZ equation with a square-well intermicellar potential and the $\bar{P}(k)$ is calculated using the modified cap-and-gown model [16] as the polymer segmental distribution function in a micelle. The observed SANS data are the product of these two functions and therefore it is clear that the interaction peak in the SANS data is primarily due to the first diffraction peak in the intermicellar structure factor.

$$x = \frac{r}{\Lambda} = k_{\max} r,$$

$$y = \frac{k}{k_{\max}},$$

it is straightforward to show that

$$\frac{k_{\max}^3 I(k)}{\langle \eta^2 \rangle} = \int_0^\infty dx 4\pi x^2 j_0(xy) \Gamma(x). \quad (4)$$

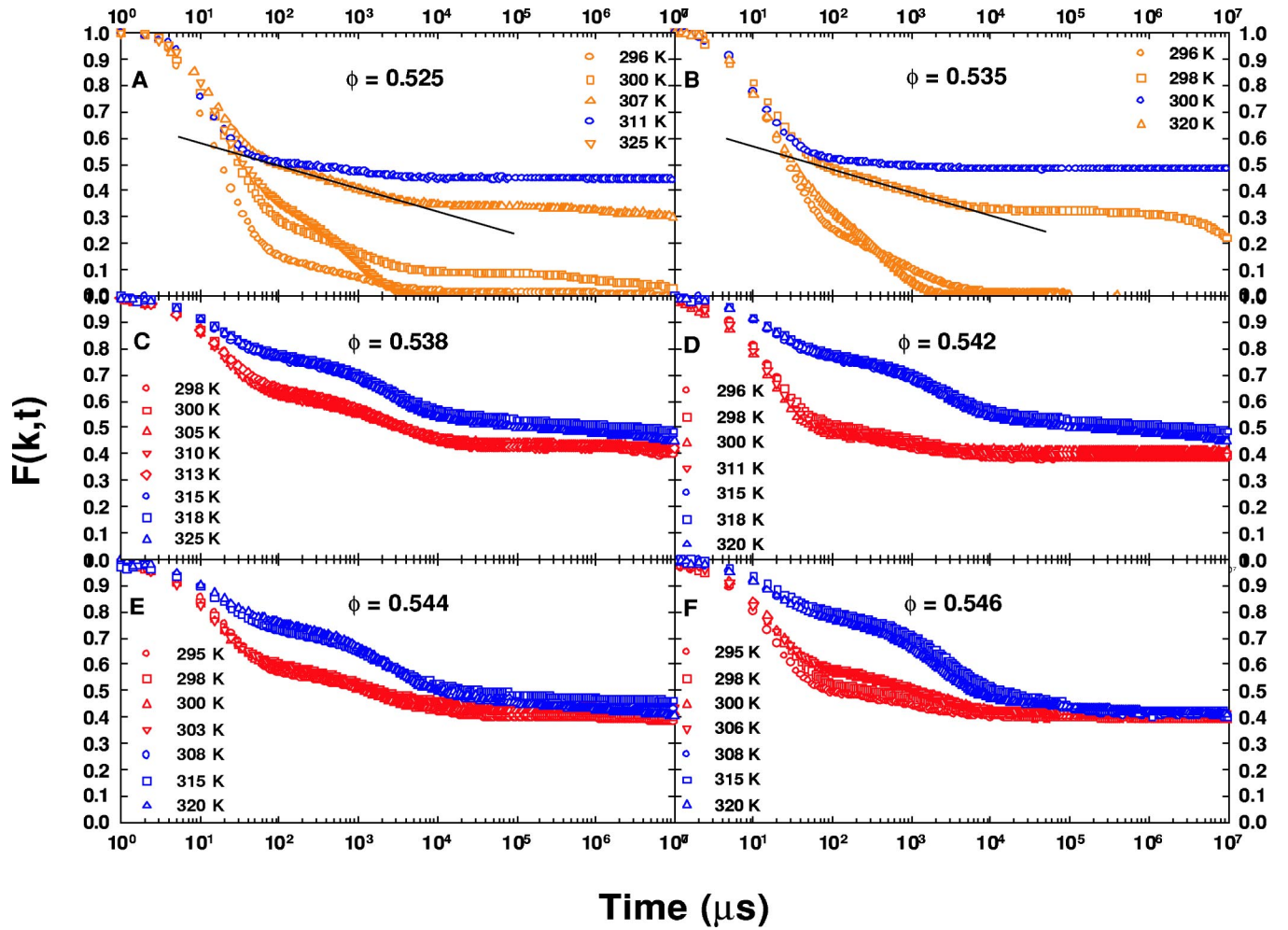


FIG. 3. (Color online) (a) and (b) represent ISFs measured at $\phi=0.525$ and $\phi=0.535$, respectively, where the liquid-to-attractive glass transition is found, as a function of temperature. In the liquid state, the long-time limit of ISF (DWF), f_k , is zero, while in the attractive glass state f_k is about 0.5. The structural arrest transition is thus characterized by a discontinuous change of f_k , called a bifurcation transition. The observed occurrence of a region of the logarithmic time dependence, preceding the plateau region for the system in the ergodic state just before the transition, is highlighted by a straight line in the linear-log plots, respectively. (c) and (d) represent ISFs measured at $\phi=0.538$ and $\phi=0.542$. According to MCT, in this volume fraction range, there is a possibility to observe glass-to-glass transition by varying the effective temperature T^* . Since the depth of the potential well, $-u$, is temperature dependent and increases on heating, the effective temperature T^* actually decreases as temperature rises, making the transition from the repulsive glass to the attractive glass possible. By comparing the long-time limit of the ISFs, the two different types of the glasses can be identified by their respective DWFs, $f_k^A \sim 0.5$ and $f_k^R \sim 0.4$. The reason for observing two different values of DWFs can be interpreted as the different degrees of localization of the density fluctuation having the wave number k , for the two types of glasses. (e) shows ISFs measured at $\phi=0.544$, where according to MCT, the long-time limit of ISF of the two glasses become identical. In our measurements, the long-time limit of ISFs of the attractive glass gradually decreases from 0.5, and gets closer to 0.4, the long-time limit of ISFs of the repulsive glass. Although the DWFs of these two types of glasses are almost identical, it is essential to recognize that there is a significant difference between the dynamics of their intermediate time relaxations. (f) shows ISFs measured at $\phi=0.546$. At this volume fraction, the long-time limit of ISFs of the attractive glass approaches closely to 0.4, which is the long-time limit of ISFs of the repulsive glass. It indicates that beyond the volume fraction 0.544, the two glasses merge into a single repulsive glass. Judging from (e) and (f), the experimentally determined volume fraction for A_3 singularity lies somewhere between $\phi=0.544$ and $\phi=0.546$.

Thus it can be seen that the scaled intensity $k_{\max}^3 I(k)/\langle \eta^2 \rangle$ is a unique function of the scaled magnitude of the scattering vector, $y = k/k_{\max}$. Therefore, if we plot the scaled intensity distributions at different temperatures as a function of y , they should collapse into one single master curve in the single-phase amorphous state.

More specifically, take Fig. 2 as an example in our case,

the physical meaning of the scale intensity $k_{\max}^3 I(k)/\langle \eta^2 \rangle$ can be interpreted as follows.

The invariant $\langle \eta^2 \rangle$ is mathematically defined as

$$\langle \eta^2 \rangle = \frac{1}{2\pi^2} \int_0^\infty k^2 I(k) dk. \quad (5)$$

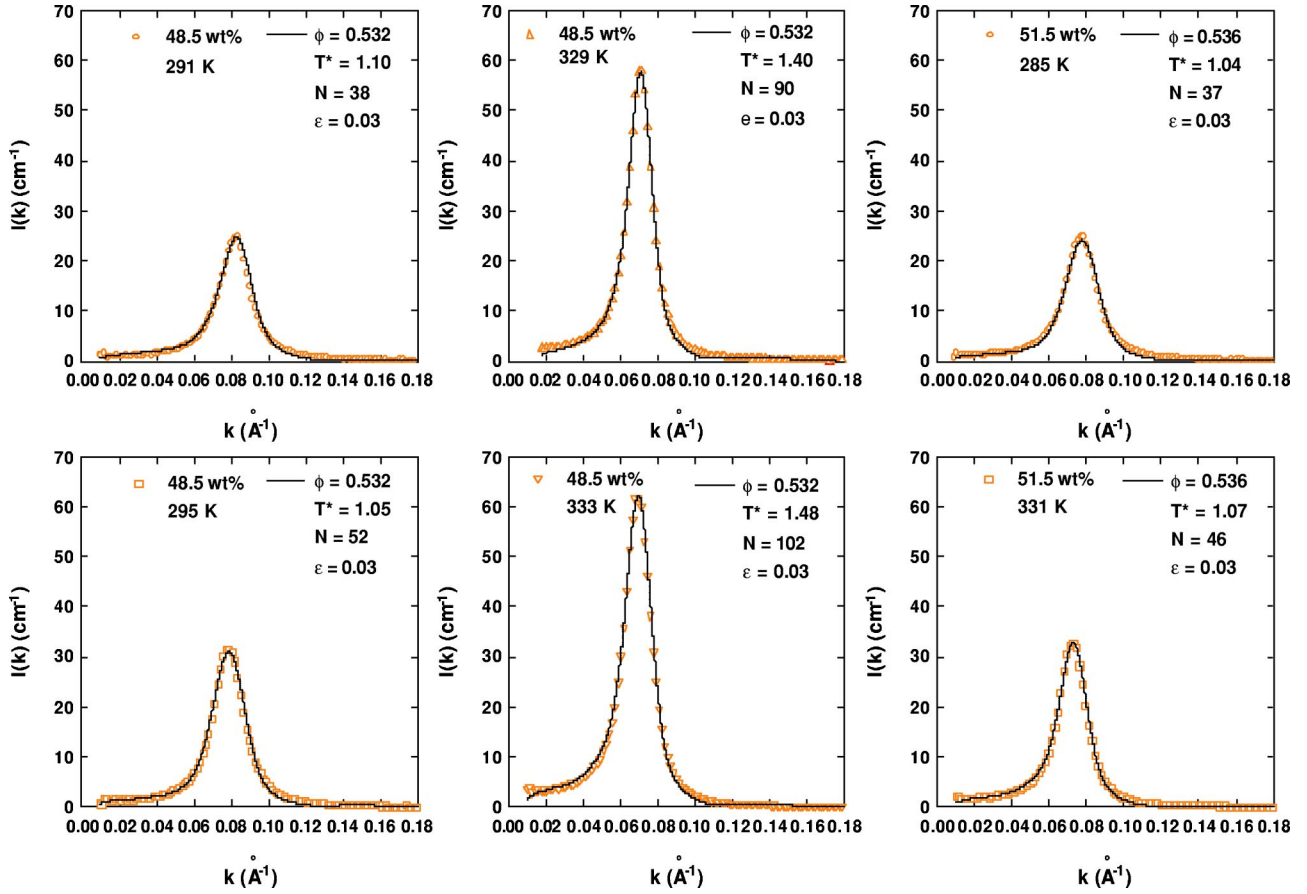


FIG. 4. (Color online) The theoretical fits to SANS data taken at NG7 SANS spectrometer at the NIST Center for Neutron Research, for Pluronic L64 micellar solutions at various concentrations and temperatures. Symbols are experimental data and lines are the fits. The fits in absolute intensity scale take into account the effects of the resolution and the incoherent scattering backgrounds. The scattering intensities increase at the higher temperature liquid phase as compared to lower temperature liquid phase and the positions of the peaks shift toward smaller k due to the enhanced self-association (larger aggregation number) as the consequence of increased hydrophobicity of the polymer segments at higher temperatures. It is important to note that from these fits we obtain unique values of four parameters: volume fraction ϕ , fractional well width ϵ , the effective temperature $T^* = k_B T / u$ and the aggregation number of the micelle N .

From Fig. 2 one can see that the minimum wave vector signaling the onset of the Porod's law is at $k_1 \sim 0.09 \text{ \AA}^{-1}$. According to the inset of Fig. 2, Porod's law $I(k) = Ak^{-4}$ is valid, when $k > k_1 = 0.09 \text{ \AA}^{-1}$. $I(k_1) = 1 \text{ cm}^{-1} = 10^{-8} \text{ \AA}^{-1}$, thus $A = 6.5 \times 10^{-13} \text{ \AA}^{-5}$. Therefore, the integral in $\langle \eta^2 \rangle$ can be divided into two parts, and the scaled intensity $k_{\max}^3 I(k) / \langle \eta^2 \rangle$ can be rewritten as

$$\begin{aligned} \frac{k_{\max}^3 I(k)}{\langle \eta^2 \rangle} &= \frac{k_{\max}^3 I(k)}{\frac{1}{2\pi^2} \int_0^\infty k^2 I(k) dk} \\ &= \frac{k_{\max}^3 I(k)}{\frac{1}{2\pi^2} \left[\int_0^{k_1} k^2 I(k) dk + \int_{k_1}^\infty k^2 I(k) dk \right]} \\ &= \frac{k_{\max}^3 I(k)}{\frac{1}{2\pi^2} \left[\int_0^{k_1} k^2 I(k) dk + \int_{k_1}^\infty k^2 \frac{6.5 \times 10^{-13}}{k^4} dk \right]} \end{aligned}$$

$$= \frac{k_{\max}^3 I(k)}{\frac{1}{2\pi^2} \int_0^{k_1} k^2 I(k) dk + 3.3 \times 10^{-13}} \quad (6)$$

Furthermore, $\langle \eta^2 \rangle$ can be evaluated numerically and the result is $4.7 \times 10^{-12} \text{ \AA}^{-4}$. Since the contribution from the Porod's part is only $3.3 \times 10^{-13} \text{ \AA}^{-4}$, which is about 7.0% of $\langle \eta^2 \rangle$, $k_{\max}^3 I(k) / \langle \eta^2 \rangle$ can thus be approximated as

$$\frac{k_{\max}^3 I(k)}{\langle \eta^2 \rangle} \approx \frac{k_{\max}^3 I(k)}{\frac{1}{2\pi^2} \int_0^{k_1} k^2 I(k) dk} \quad (7)$$

As we see from Fig. 2, $\bar{P}(k)$ varies slowly within the k range of the first diffraction peak of $S(k)$, and is negligibly small beyond k_1 , the scale intensity $k_{\max}^3 I(k) / \langle \eta^2 \rangle$ can thus be well approximated by substituting Eq. (2) into Eq. (7) and canceling the common factor $\bar{P}(k)$ from the numerator and the denominator of the equation to obtain the result:

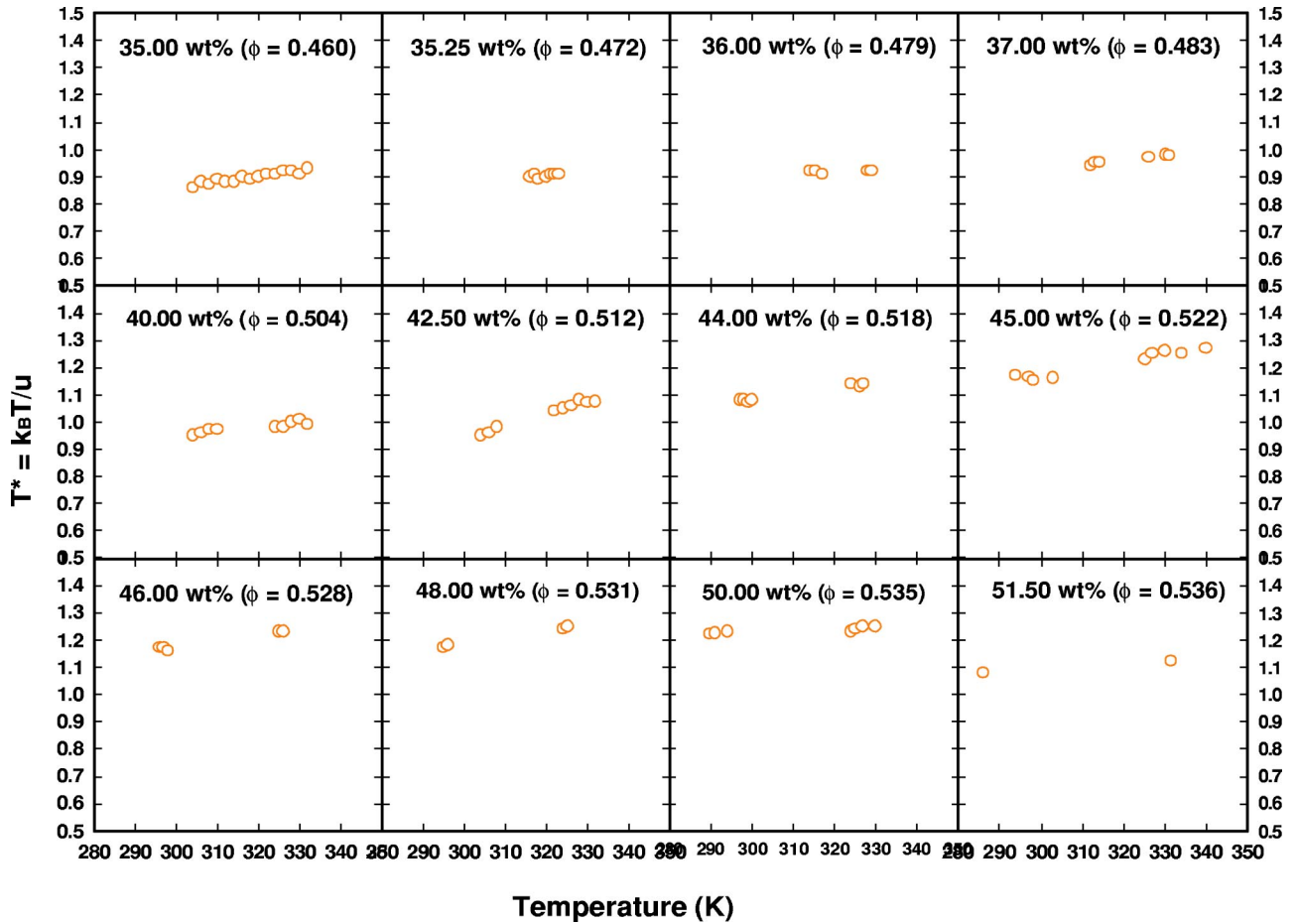


FIG. 5. (Color online) The effective temperature T^* of liquid state as a function of temperature, obtained by fitting SANS intensity distributions from different concentrations. For the indicated concentrations, T^* generally increases as temperature increases except in the glass region which appears as a gap in the figure.

$$\frac{k_{\max}^3 I(k)}{\langle \eta^2 \rangle} \approx \frac{k_{\max}^3 S(k)}{\frac{1}{2\pi^2} \int_0^{k_1} k^2 S(k) dk} \quad \text{for } k \leq k_1. \quad (8)$$

Therefore, without losing generality, the scale intensity is proportional to the interparticle structure factor $S(k)$ in the region of its first diffraction peak. Examples and discussion of the scaling plots are given in the following section.

V. RESULTS AND DISCUSSION

A. Intermediate scattering function measured by photon correlation spectroscopy

To test the phase behavior predicted by MCT calculations for an AHS system, ISFs were measured for a set of volume fractions within the interval $0.525 < \phi < 0.546$, where the reentrant phenomena of the glass-to-liquid-to-glass transition, glass-to-glass transition and the A_3 singular point were predicted for the case of $\varepsilon=0.03$, as shown in Fig. 1. Figure 3(a) and 3(b) show ISFs obtained by PCS for two volume fractions $\phi=0.525$ and $\phi=0.535$, respectively, at different temperatures. As can be seen, on increasing the temperature, the

system, starting from a liquid state at a lower temperature, where the ISF decays to zero at long time, approaches a KGT, characterized by a diverging α relaxation time. At KGT the ISF tends to a finite plateau at long time [$F(k, t \rightarrow \infty) = f_k > 0$]. Just before such an ergodic-to-nonergodic transition taking place, the ISF measured in an ergodic state exhibits a logarithmic relaxation (indicated by a straight line fit) at an intermediate time followed by a power-law decay before the final α relaxation sets in. This is in agreement with the MCT prediction. The nonergodic state ($T=300$ K, for $\phi=0.535$), as indicated by the ISF having a finite plateau at long time, represents the attractive glass for which the Debye-Waller factor (DWF, the height of the plateau) f_k is about 0.5. As discussed above, an important prediction of the MCT calculation for an AHS is a suggestion that there exists an attractive branch of KGT line near the cusp singularity separating two different glass phases [22,10]. Motivated by this prediction, we extended the study of the micellar system to higher temperatures. Starting from a glass state, upon increasing the temperature further, the measured ISF reveals a surprising reentry from the glass to the liquid state, as seen by the ISF again decaying to zero at higher temperatures.

The ISFs measure at $\phi=0.538$ and $\phi=0.540$, where the

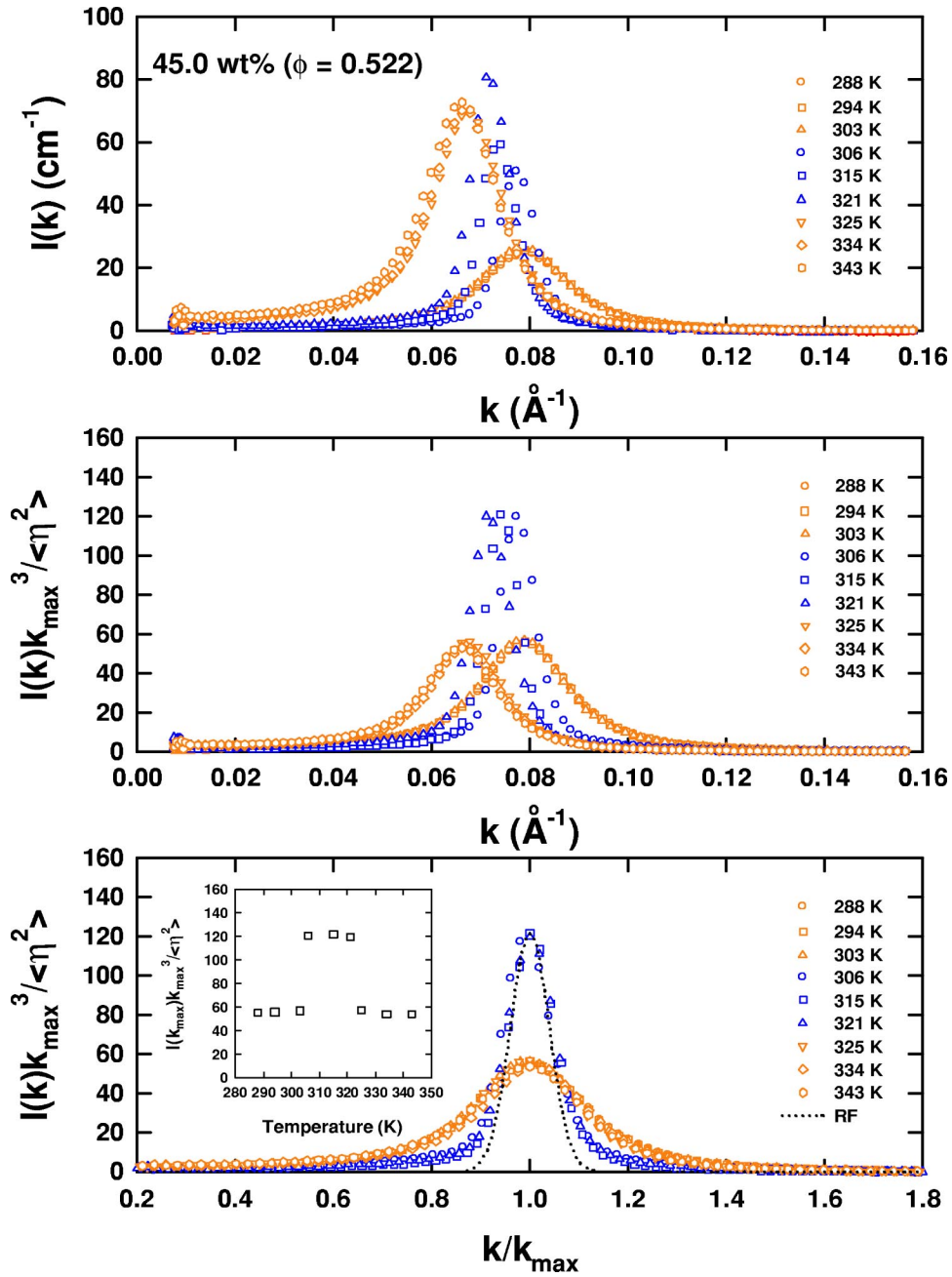


FIG. 6. (Color online) SANS intensity distributions and their scaling plots at $\phi=0.522$, where the liquid-to-glass-to-liquid transition is observed, at a temperatures range spanning 288 K–343 K. The top panel shows the SANS intensity distributions as a function of k . The broader peaks (from 288 K to 303 K, 325 K to 343 K) represent the liquid states and the narrower ones (from 306 K to 321 K) represent the glassy state. The scattering intensities increase at the higher temperature liquid phase (the left-hand side peak, from 325 K to 343 K) as compared to lower temperature liquid phase (the right hand-side peak, from 288 K to 303 K) and the positions of the peaks shift toward smaller k due to the enhanced self-association (larger aggregation number) as a consequence of increased hydrophobicity of the polymer segments at higher temperatures. The scaling plots of SANS intensity distributions are shown in the two bottom panels. It is seen clearly that there are two distinct degrees of disorder (judging from the width of the peak), which depend on temperature. While the narrower peak, which is resolution limited, represents the glassy state, the broader peak, which is much broader than the resolution, represents the liquid state with a broader distribution of the interparticle distances. The inset shows the peak height of the scaling plots as a function of temperature. The variation of the peak heights indicates the reentrant liquid-to-attractive glass-to-liquid transition.

glass-to-glass transition is predicted, are given in Figs. 3(c) and 3(d). In the two-length-scale AHS, aside from the volume fraction ϕ , the glass transition can be triggered by varying the effective temperature T^* as well. Due to the fact that

the depth of the potential well, $-u$, is temperature dependent and increases on heating to a certain extent, the effective temperature T^* actually decreases as temperature rises for certain interval of temperatures. Variation of temperature

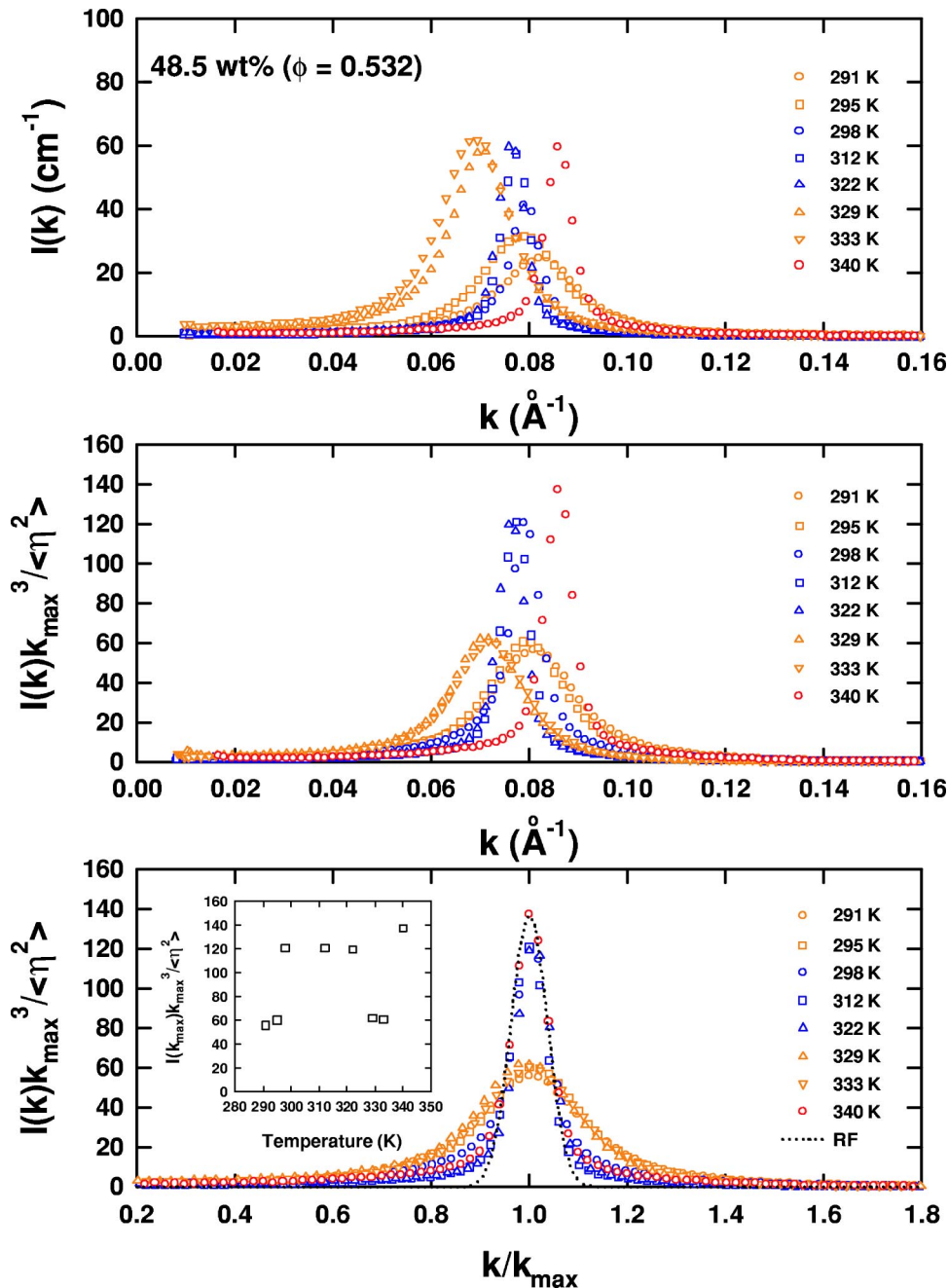


FIG. 7. (Color online) SANS intensity distributions and the scaling plots at $\phi=0.532$, at a temperature range spanning 290 K–340 K. The top panel shows the SANS intensity distributions as a function of k . It shows the similar features as the top panel of Fig. 6: As temperature increases, a liquid-to-glass-to-liquid transition is observed. However, as the temperature is increased to 340 K, another disordered state peaked at $k=0.082 \text{ \AA}^{-1}$ is observed. The other two panels show the scaling plots of the SANS intensity distributions. A temperature-dependent degree of disorder characterizes the system. While the narrowest peak (340 K) is resolution limited, the slightly broader peak (from 298 K–322 K) is also nearly resolution limited, but lower in intensity. From the inset given in the bottom panel, the liquid-to-glass-to-liquid-to-glass reentrant transition can be seen clearly.

thus makes the transition between two distinct types of glasses possible. Because the long-time limit of the ISF (DWF) reflects the degree of localization of the density fluctuation of a given wave vector, these two different types of glasses, if they have different degrees of local disorder, can be identified by their different values of DWF. From Figs. 3(c) and 3(d) it is obvious that all the ISFs can be grouped into two distinct sets of curves having two different values of DWF—one at $f_k=0.5$ (attractive glass) and the other at $f_k=0.4$ (repulsive glass). Figures 3(c) and 3(d) confirm the predicted glass-to-glass transition.

Figure 3(e) shows the ISFs measured at $\phi=0.544$, which, according to MCT, is the end point of the predicted glass-to-glass transition line and therefore the long-time limit of ISF

of the two glasses should become identical at this point. Our measured ISFs verify this prediction, showing two nearly identical values of DWF, for the two glassy states, with an average value of $f_k \sim 0.45$. Although the DWFs of these two types of glasses are identical, it is important to recognize that there is a significant difference between the dynamics of their intermediate time relaxations (the β relaxation region).

The ISFs measured at $\phi=0.546$, which is a volume fraction beyond the A_3 point, is shown in Fig. 3(f). This figure shows similar features as in Fig. 3(e), with a merged DWF of $f_k \sim 0.4$. It strongly hints that beyond the volume fraction $\phi=0.544$, the system exists in a repulsive glass state. It is interesting to note here a critical pointlike characteristics of the A_3 point.

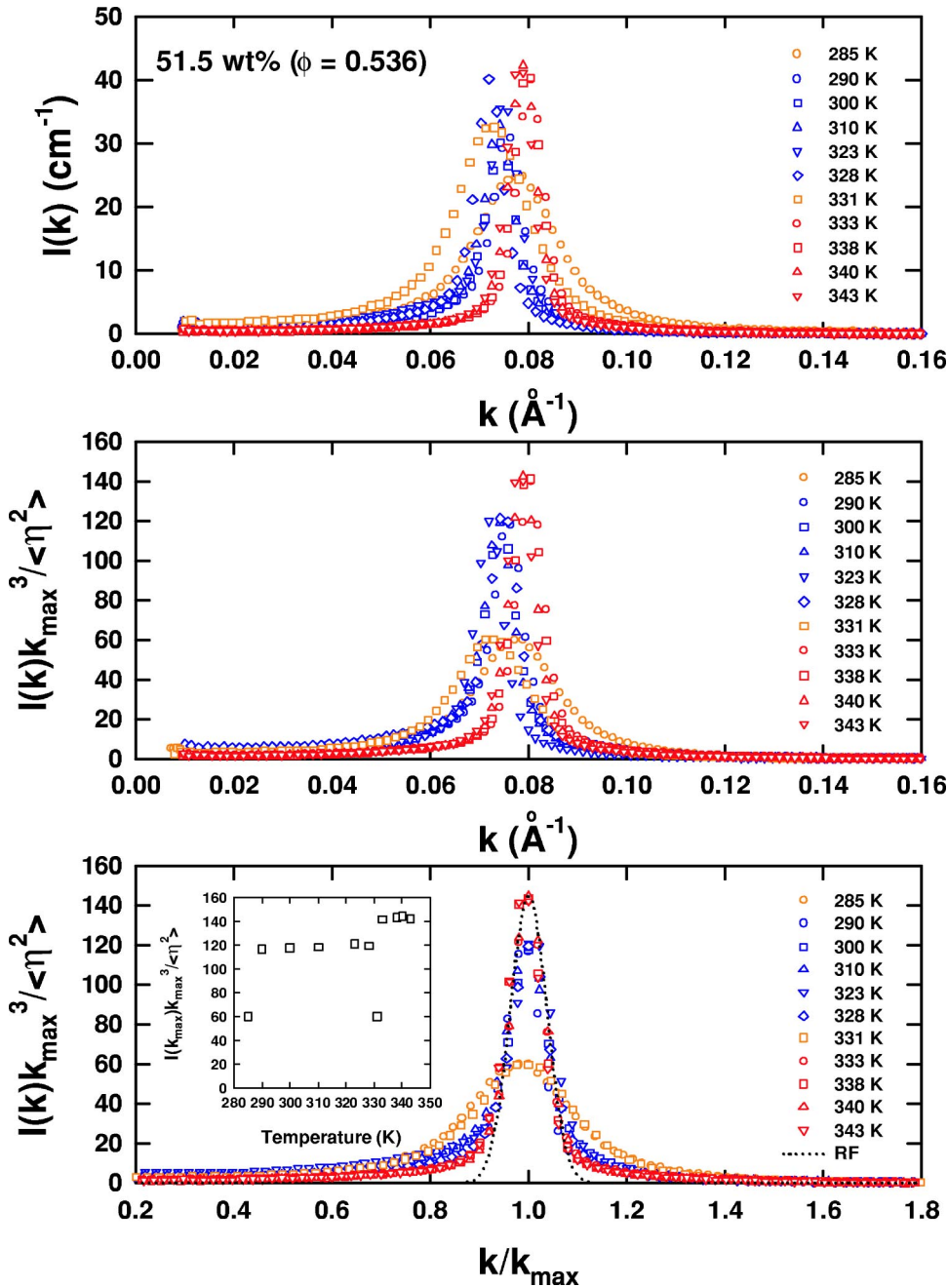


FIG. 8. (Color online) SANS intensity distributions and the scaling plots at $\phi=0.536$, at a temperature range spanning 285 K–343 K. It exhibits all the features found in Fig. 7. However, the high temperature liquid state is only observed at 331 K, when the temperature increases to 333 K, the system transits to the repulsive glass state. Figure 7 and this figure together show a convincing evidence of the predicted reentrant glass-to-liquid-to-glass transition. The only difference between them is that the transition temperatures between different amorphous states are different. The inset shows the reentrant transition more clearly.

B. Fitting results of SANS data

Small-angle neutron-scattering experiments were performed on Pluronic L64/D₂O micellar solutions at different concentrations and temperatures. These experiments were carried out using NG7 SANS spectrometer at NIST Center for Neutron Research and the SAND station at IPNS, Argonne National Laboratory. Part of the experimental results as well as their theoretical fits are given in Fig. 4. Symbols are experimental data and lines are the fits. The fits are in an absolute intensity scale taking into account the effects of the instrumental resolution and the incoherent background. It can be seen that for samples at both volume fractions, $\phi=0.532$ and $\phi=0.536$, the peak intensity is generally higher for the sample at the higher temperature liquid phase. Furthermore, the position of the peak shifts toward smaller k

as temperature increases. This is due to the enhanced self-association of the micelle (larger aggregation number) as the consequence of the increased hydrophobicity of the polymer segments at higher temperatures. It is important to note here that in spite of the micelle growth as temperature increases, SANS data analyses show that the volume fraction of the micelles remains constant, for a given weight fraction of L64, at all temperatures studied.

Figure 5 summarizes the variation of the fitted effective temperature parameter T^* , as a function of temperature T , for several volume fractions studied. It can be seen clearly that as the T increases, the T^* also increases. There are no data shown in the glass regions, which appear as gaps in the plots, due to lack of an appropriate theory for the structure factor of a system in a nonergodic state, showing the effect of aging process.

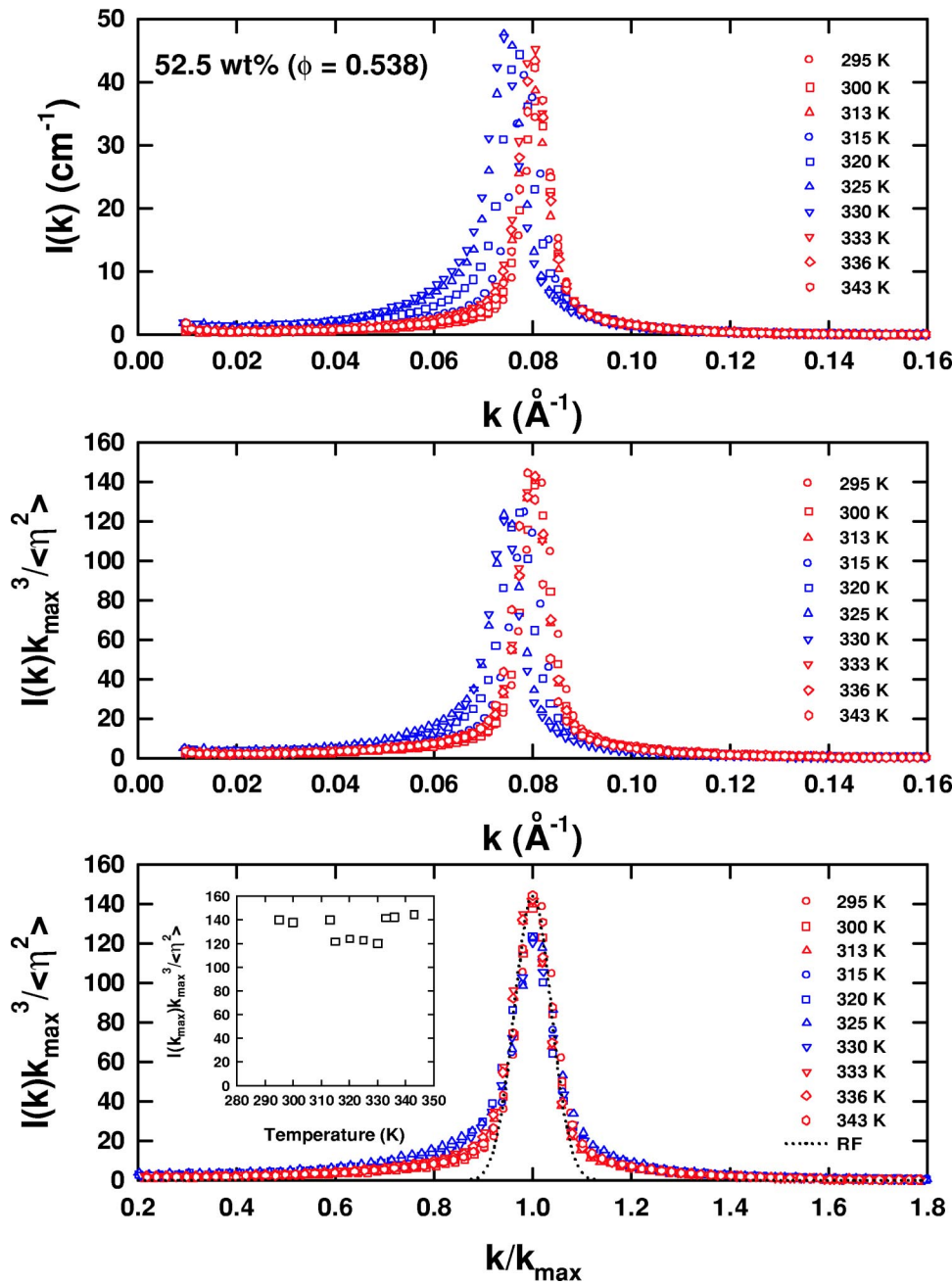


FIG. 9. (Color online) SANS intensity distributions and the scaling plots at $\phi=0.538$, at a temperature range spanning 295 K–343 K. From the SANS intensity distributions shown in the top panel, it can be seen that the much broader peaks (liquid state) disappear. Variation of temperature triggers the transition between the two amorphous solid states with different degrees of disorder. The variation of the peak heights of the scaling plots as a function of temperature given in the inset shows a reentrant repulsive glass-to-attractive glass-to-repulsive glass transition.

C. Scaling plots of SANS data

Figure 6 shows a series of SANS intensity distributions and their associated scaling plots for the 45wt% concentration sample at different temperatures. The volume fraction of micelles for this polymer concentration is determined by SANS data analysis to be at $\phi=0.522$, independent of temperature. In view of the fact that the 2D SANS patterns show an isotropic ring, we conclude that the sample stays amorphous in the entire temperature range studied at this concentration. Looking carefully at the SANS intensity distributions as a function of temperature given at the top panel, one already sees clues showing the kinetic glass transition: Judging from the width of the peak, the intensity distributions at different temperatures can be categorized into two groups—a sharp one and a broad one. The situation becomes clearer by

analyzing the intensity distributions using the scaling plots. SANS intensity distribution $I(k)$ is proportional to the product $\bar{P}(k)S(k)$, where $\bar{P}(k)$ is the decaying Gaussian-like peak centered around $k=0$. Thus the above product results in a single peak, reflecting the position and the height of the first diffraction peak of $S(k)$, as explained in Sec. IV. It is well known that the position of the first diffraction peak of $S(k)$ reflects the mean interparticle separation of the system and the height of the peak reflects the degree of local order surrounding a typical particle. Thus the height and the width of the scaling peak can be used to visualize the degree of local order surrounding a given particle in an amorphous state. Therefore, a sudden sharpening at given temperature signals the onset of the liquid-to-amorphous solid transition. As one can see from the two lower panels, there are two

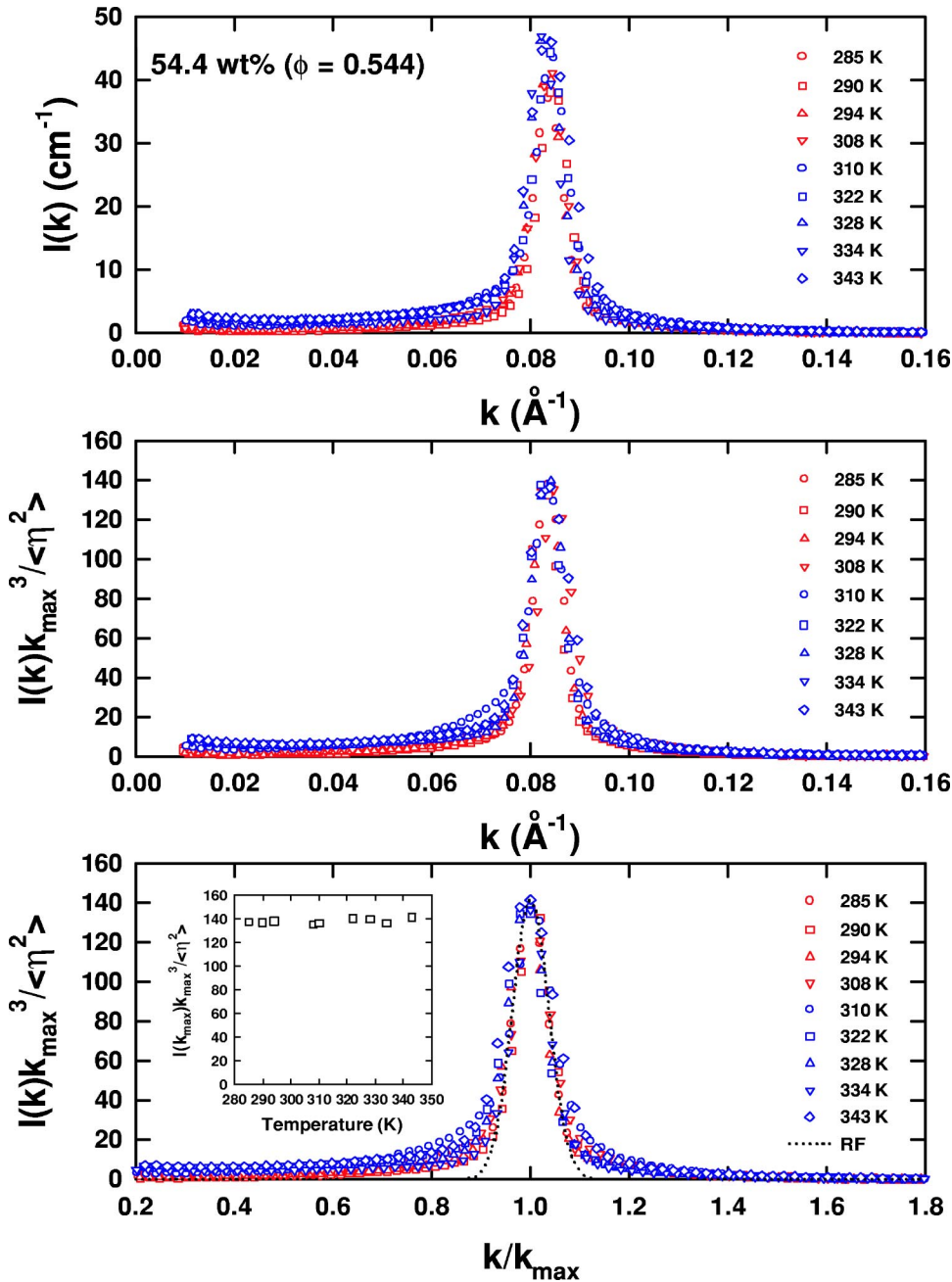


FIG. 10. (Color online) SANS intensity distributions and the scaling plots of SANS intensities at $\phi=0.544$, which is predicted to be the volume fraction where the A_3 singularity point is located, at a temperature range spanning 285 K–343 K. From the top panel, it can be seen that all the peaks of the SANS intensity distributions are located at the same k value (0.0836 \AA^{-1}). Furthermore, from the scaling plots shown in the two bottom panels, it can be seen that all the scaled intensities collapse into one single master curve. It suggests that the two different types of glasses become identical in their local structure at this volume fraction. The inset given in the bottom panel shows that all the scaling peaks have an identical height (about 140), indicating the two glasses indeed have the same degree of local order.

distinct degrees of disorder, which depend on temperature. While the narrower peak, which is resolution limited, represents the glassy state and the broader peak, which is much broader than the resolution, represents the liquid state with a broader distribution of the interparticle distances. This figure indicates that the system shows a reentrant liquid-to-attractive glass-to-liquid transition as temperature increases. The sharpness of the scaling peaks which are resolution limited indicates that the nearest neighbor distance in the glassy state (ranging from 306 K to 321 K) is more uniform than that in the liquid state (from 288 K to 303 K, 325 K to 343 K). The inset shows the peak height of the scaling plots as a function of temperature. The variation of the peak heights indicates the reentrant liquid-to-attractive glass-to-liquid transition.

SANS intensity distributions and their scaling plots for a sample at 48.5 wt %, or $\phi=0.532$, at a series of temperatures ranging from 291 K to 340 K are shown in Fig. 7. The scenario is similar to the previous example: A temperature-dependent degree of disorder again characterizes the system. As the temperature rises, the system experiences a liquid-to-glass-to-liquid transition. However, in addition to all the similarities, when the temperature increases to 340 K, the system is driven into another glassy state peaked at $k = 0.082 \text{ \AA}^{-1}$. From the scaling plots shown in the bottom two panels, one can tell the differences between these two disordered glassy states. While the narrowest peak (340 K) is resolution limited, the slightly broader peak (from 298 K to 322 K) is also nearly resolution limited, but lower in the scaled intensity. Since the difference in local structures of

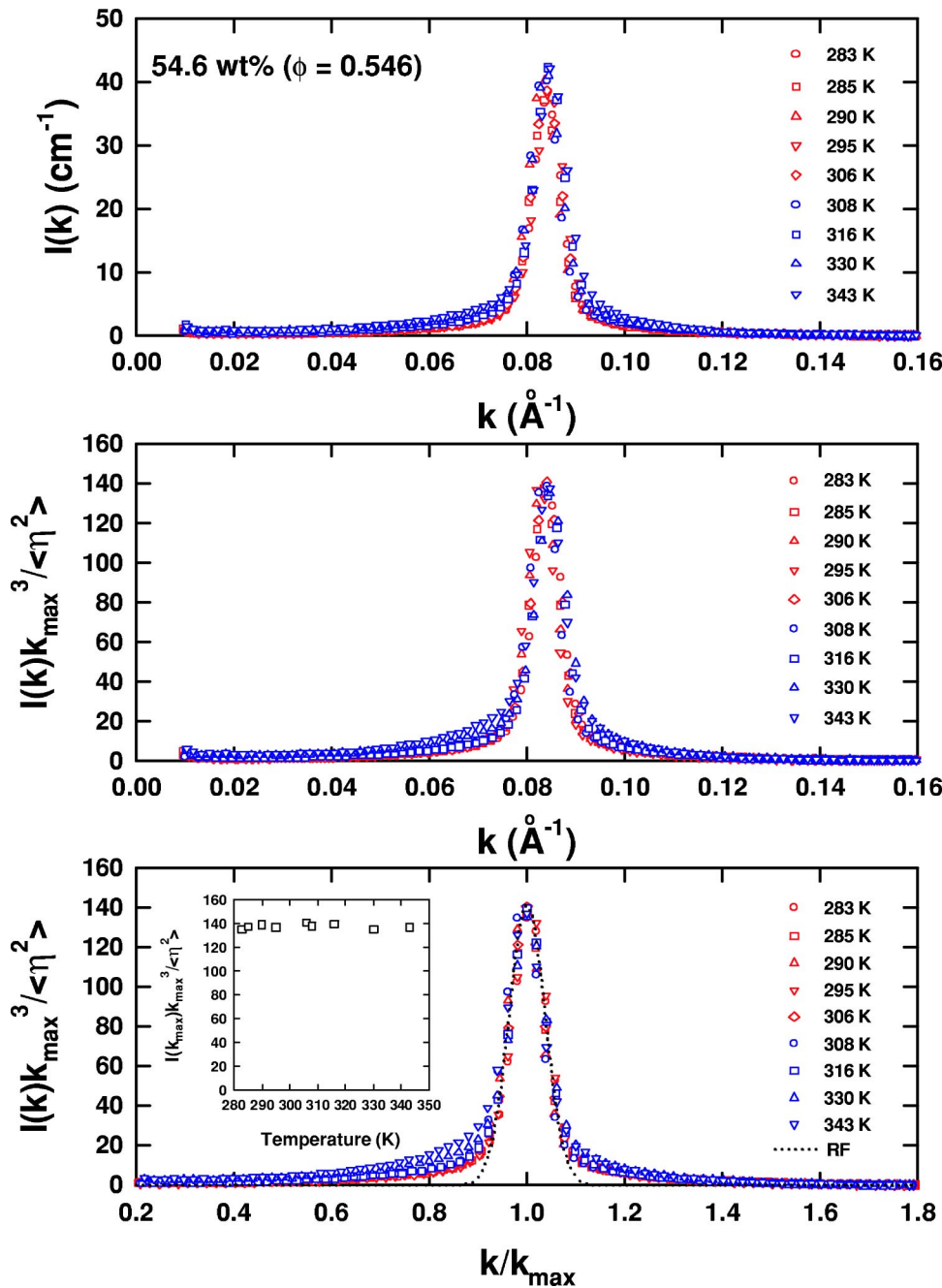


FIG. 11. (Color online) SANS intensity distributions and the scaling plots of SANS intensities at $\phi=0.546$, a volume fraction beyond the A_3 point, at a temperature range spanning 283 K–343 K. As Fig. 10, all the scaled intensities are again characterized by a unique length scale and collapse into one single master curve, independent of temperature, showing identical local structure of these two glasses.

different states is reflected in their scaling plots (see discussion in Sec. IV), we conclude that the degrees of disorder are different for these two amorphous states. It can be interpreted that by varying the temperature, the system shows a liquid-to-glass-to-liquid-to-glass transition.

Figure 8 shows the same plots taken at concentration of 51.5 wt%, or $\phi=0.536$, for different temperatures. Generally, it delivers the same message as Fig. 7: it shows the reentrant transition. However, it can be seen that the transition temperatures between different states for these two different volume fractions are different; especially at the high temperature region. For example, for the case of $\phi=0.536$, the high temperature liquid state is observed only at 331 K. When the temperature increases to 333 K, the system transits to the repulsive glass state. In order to make this point more clear,

the peak heights of the scaling plots as a function of temperature are shown in the insets of the bottom panels of Figs. 7 and 8. The transition temperatures between different amorphous states can be visualized clearly in the figure. These two figures show a firm evidence of the reentrant glass-to-liquid-to-glass transition which is in good agreement with the prediction of MCT for an AHS system. We would like to mention here that the KGT boundaries determined by SANS agree with the results obtained from the latest specific heat measurements [25].

According to the MCT calculations for an AHS with sufficiently short-range attraction, a glass-to-glass transition is predicted [10]. Although the transitions between different amorphous glassy states are not uncommon in pure substances such as H_2O , Si, Ge [23], yet there is no detail in-

vestigation of the glass-to-glass transition in a micellar system so far except for some recent reports [16,17]. Combining with the PCS [see Figs. 3(c) and 3(d)], a concrete evidence of such a transition in a micellar system was revealed by SANS. From SANS intensity distributions, taken at $\phi=0.538$, shown in Fig. 9, one can see that the much broader peaks (liquid state) disappear and variation of temperature triggers the transition between the two amorphous solid states with different degrees of disorder. By increasing the temperature, the variation of the peak heights of the scaling plots shown in the inset shows a reentrant repulsive glass-to-attractive glass-to-repulsive glass transition.

Perhaps the most important prediction of the AHS system is the existence of the end point of the glass-to-glass transition line, the so-called A_3 singularity. Comparing with the critical point of the equilibrium states, certain degree of similarity between them can be found. Therefore, it is intriguing to speculate the extent to which one can draw the analogy between the A_3 singularity and the ordinary equilibrium critical point. In the case of $\varepsilon=0.03$, the volume fraction of the A_3 point is predicted to be $\phi(A_3)=0.544$. SANS intensity distribution and its associated scaling plot are shown in Fig. 10. As one can see, all the scaling intensity curves collapse into one single master curve, indicating that the first diffraction peaks of the structure factor for all states are identical. It suggests that the local structures of the two glasses are identical. The inset given in the bottom panel shows that all the scaling peaks have the identical height (about 140), indicating that the two glasses indeed have same degree of local order.

Increasing ϕ further to 0.546 (Fig. 11), all the scaled intensities are again characterized by a unique temperature-independent length scale and collapse into one single master curve, independent of temperature, showing an identical local structure of the two glasses. This is the proof that the MCT predictions are accurate.

The phase diagram shown in Fig. 12 summarizes the essential results of the extensive SANS and PCS data analyses. It contains the known equilibrium, liquid-to-hexagonal crystalline phase boundary (solid line) [24], the experimentally determined KGT lines (dash lines) and the phase points where parts of the experimental data are taken (symbols). This figure shows several important information about this system: First, only the metastable attractive glass is observed within the region where the true lowest free energy state is the hexagonal liquid crystalline phase. Next, the repulsive glass only exists in the region where the volume fraction is larger than 0.536. It is interesting to see that there is a pocket of the attractive glass imbedded in-between two separate repulsive glass regions spanning the volume fraction range between 0.536 and 0.544, where the reentrant glass-to-glass transition is observed. Furthermore, from Figs. 3, 10, and 11, it is important to note that the two different glasses become identical in their local structures and the long-time dynamics when the volume fraction exceeds $\phi(A_3)=0.544$. Furthermore, judging from the DWF and the peak height of the scaled intensity, the merged identical glassy state is the repulsive glass.

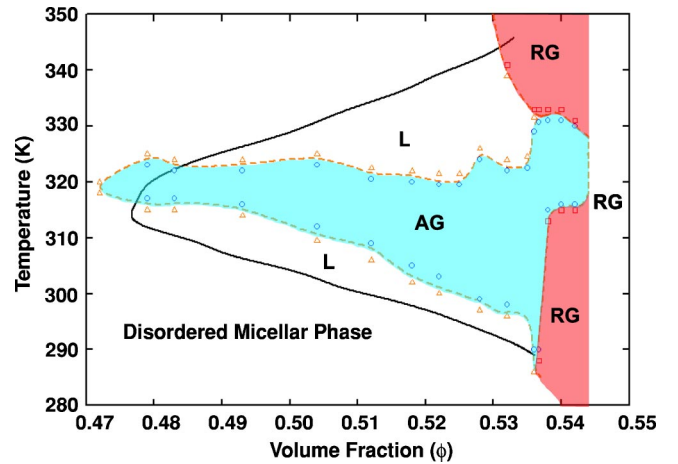


FIG. 12. (Color online) The experimental phase diagram of $L64/D_2O$ micellar system. The solid line represents the equilibrium phase boundary of disorder micellar liquid states and the hexagonal liquid crystalline states [24]. The dash line represents the kinetic glass transition boundary which is determined by SANS and PCS. The symbols represent the phase points where parts of the experimental data were taken. The triangles represent liquid state (L), the circles the attractive glass (AG), the squares the repulsive glass (RG). This figure depicts several important information about this system: Within the region where the true ground state is the hexagonal liquid crystalline phase, only the metastable attractive glass is observed. The repulsive glass is found in the region where the volume fraction is larger than 0.536. It is interesting to see that there is a pocket of the attractive glass imbedded in between two separate repulsive glass regions spanning the volume fraction range between 0.536 and 0.544. Furthermore, it is important to note that the two different glasses become identical in their local structures and the long-time dynamics when the volume fraction exceed $\phi(A_3)=0.544$.

VI. CONCLUSIONS

In summary, we used photon correlation spectroscopy to verify the fact that $L64/D_2O$ micellar system follows the overall structural arrest transition behavior predicted by the MCT, calculated using a square-well potential with a short-range attraction relative to the micellar size. In particular, we show experimentally the existence of a glass-to-glass transition line which starts at point C^* , where the two glass phases and the liquid phase coexist, and ends at point A_3 , where the two glass phases merge [17]. Our SANS experiment further shows that while the local structures of the attractive and the repulsive glasses are in general different, they become identical at the predicted volume fraction of the A_3 singularity, independent of temperature. However, our PCS results indicate that the relaxation of the two glasses are different in the intermediate time region even at the A_3 point. The central result of this paper is the use of the SANS method to pinpoint the exact volume fractions where the C^* point and the A_3 singularity are located [10] and furthermore, to verify that for volume fractions beyond the A_3 point, the system remains in the repulsive glass phase. We are able to map out the whole structural arrest transition boundaries in

the $L64/D_2O$ micellar system using SANS method alone. From SANS experiments, we observe a significant difference in the local structure when crossing the KGT boundaries at various temperatures for all the volume fractions studied. It is our conjecture that our SANS data are reflecting the ageing effect of the sample in the time scale of our measurements. We are in the process of investigating the time evolution of SANS intensity distributions at the present time.

ACKNOWLEDGMENTS

The research at MIT was supported by a grant from Materials Science Division of U.S. DOE, Grant No. DE-FG02-90ER45429. The research in Messina was supported by INFN-PRA98 and MURST-PRIN2000. We are grateful to NIST CNR and IPNS (ANL), respectively, for granting the beam time of NG7 SANS and of SAND station and to Dr. Papanan Thiagarajan and Deny Wozniak for technical assistance.

-
- [1] D.H. Everett, *Basic Principles of Colloid Science* (Royal Society of Chemistry, Letchworth, UK, 1988).
- [2] K. Dawson, *Curr. Opin. Colloid Interface Sci.* **7**, 218 (2002).
- [3] W. Götze, in *Liquids, Freezing and the Glass Transition*, edited by J.P. Hansen, D. Levesque, and J. Zinn-Justin (North Holland, Amsterdam, The Netherlands, 1991), p. 287.
- [4] W. Götze and L. Sjögren, *Rep. Prog. Phys.* **55**, 241 (1992).
- [5] W. Götze, *J. Phys.: Condens. Matter* **11**, A1 (1999).
- [6] P.N. Pusey and W. van Meegen, *Phys. Rev. Lett.* **59**, 2083 (1987).
- [7] M. Fuchs, *Transp. Theory Stat. Phys.* **24**, 855 (1995).
- [8] W. van Meegen and S.M. Underwood, *Phys. Rev. E* **49**, 4206 (1994).
- [9] E. Bartsch, M. Antonietti, W. Schupp, and H. Sillescu, *J. Chem. Phys.* **97**, 3950 (1992).
- [10] K. Dawson, G. Foffi, M. Fuchs, W. Götze, F. Sciortino, M. Sperl, P. Tartaglia, Th. Voigtmann, and E. Zaccarelli, *Phys. Rev. E* **63**, 011401 (2001).
- [11] J. Bergenholtz and M. Fuchs, *Phys. Rev. E* **59**, 5706 (1999).
- [12] J. Bergenholtz and M. Fuchs, *J. Phys.: Condens. Matter* **11**, 10171 (1999).
- [13] T. Eckert and E. Bartsch, *Phys. Rev. Lett.* **89**, 125701 (2002).
- [14] K.N. Pham, A.M. Puertas, J. Bergenholtz, S.U. Egelhaaf, A. Moussaid, P.N. Pusey, A.B. Schofield, M.E. Cates, M. Fuchs, and W.C.K. Poon, *Science* **296**, 104 (2002).
- [15] F. Mallamace, P. Gambadauro, N. Micali, P. Tartaglia, C. Liao, and S.H. Chen, *Phys. Rev. Lett.* **84**, 5431 (2000).
- [16] Wei-Ren Chen, Sow-Hsin Chen, and Francesco Mallamace, *Phys. Rev. E* **66**, 021403 (2002).
- [17] Sow-Hsin Chen, Wei-Ren Chen, and Francesco Mallamace, *Science* **300**, 619 (2003).
- [18] S.H. Chen, C. Liao, E. Fratini, P. Baglioni, and F. Mallamace, *Colloids Surf., A* **183-185**, 95 (2001).
- [19] C. Liao, S.M. Choi, F. Mallamace, and S.H. Chen, *J. Appl. Crystallogr.* **33**, 677 (2000).
- [20] L. Lobry, N. Micali, F. Mallamace, C. Liao, and S.H. Chen, *Phys. Rev. E* **60**, 7076 (1999).
- [21] Y.C. Liu, S.H. Chen, and J.S. Huang, *Phys. Rev. E* **54**, 1698 (1996).
- [22] L. Fabbian, W. Götze, F. Sciortino, P. Tartaglia, and F. Thierly, *Phys. Rev. E* **59**, R1347 (1999).
- [23] E.G. Ponyatovsky and O.I. Barkalov, *Mater. Sci. Rep.* **8**, 147 (1992).
- [24] K.Z. Zhang, B. Lindman, and L. Coppola, *Langmuir* **11**, 538 (1995).
- [25] F. Mallamace, C. Ferrari, A. Mazzaglia, P. Salvetti, E. Tombari and S.H. Chen (unpublished).